5-6-2020

Heat transfer and melt dynamics of spherical ice particles impacting a heated water bath

Kate Baskin
Washington University in St. Louis

Katharine M. Flores
Washington University in St. Louis

Patricia Weisensee
Washington University in St. Louis

Heat transfer and melt dynamics of spherical ice particles impacting a heated water bath

Katherine Baskin[1], Katharine M. Flores[1,2], Patricia B. Weisensee[1,2*]

[1] Department of Mechanical Engineering & Materials Science, Washington University in St. Louis, USA

[2] Institute of Materials Science and Engineering, Washington University in St. Louis, USA

[*] corresponding author: p.weisensee@wustl.edu

1. Abstract

In metallic additive manufacturing using direct energy deposition, particles and melt pool undergo complex interactions, including particle impact, penetration, and melting. The spatio-temporal evolution of these processes dictates the final material properties and workpiece quality. However, due to the opaqueness of metallic melt pools, in-situ visualization is nearly impossible. To model this system, we use high-speed imaging to investigate the heat transfer and melting dynamics of spherical ice particles ($D \approx 2$ mm) impacting heated water baths of varying temperatures (23 – 70°C) with velocities ranging from 0.8 to 2.1 m/s. To visualize the outflow of molten ice, representative of mixing and material homogeneity, the particles were colored with food dye. We show that after impact, molten liquid forms an annular plume travelling downwards in the bath, until hitting the bottom of the enclosure and expanding radially. Due to positive buoyancy forces, unmolten ice particles rise to the top of the water bath, where they fully melt. As temperatures increase, we observe random particle movement, indicating the presence of convective currents. Through video analysis, we examine the relationships between bath temperature, impact velocity, and heat transfer. As expected, increasing the bath temperature decreases the total melt time of the ice particle. Interestingly, the impact velocity has only a minor effect on the melting time. Using non-dimensional analysis, we derive an expression for the correlation between Nusselt and Jakob numbers. Outcomes from this work can be used to match characteristic time scales during additive manufacturing to tailor material properties.

2. Introduction

Additive manufacturing (AM) comprises a fast evolving and revolutionary set of technologies for manufacturing components with complex shapes, typically for applications requiring low-to-moderate part counts. Evolving from the ubiquitous "3D printing" technologies used to construct model or prototype parts from polymeric fibers, industrial-scale methods now exist that can construct high-quality, production-scale parts from metals and ceramics. A subset of AM methods, direct energy deposition (DED), uses a concentrated energy source such as a laser or electron beam to create a melt pool on the surface of a workpiece. A stream of solid powder particles is fed into the melt pool, which then quenches rapidly as the energy source and powder stream raster across the surface of the workpiece to create a newly deposited layer of material. Processing parameters, including the power of the energy source, its travel speed relative to the workpiece, and the composition and flow rate of the powder, can be adjusted to control the local thermal conditions during deposition and thereby control the local microstructure and composition of the final part (1–4).

While the highly localized nature of the DED process provides the opportunity to optimize the material microstructure and composition as a function of position within the part, numerous questions remain about the physical processes occurring within the melt pool during deposition. These influence both the evolution of the microstructure and the formation of defects, including voids or undesirable compositional variations associated with incomplete melting or mixing of the powder in the melt pool (5,6). Unfortunately, in-situ characterization of the melt pool and powder particle dynamics remains a challenge due to the inaccessibility and opaqueness of the melt pool (7–9).

In the present work, we construct a model system to investigate the particle-melt pool interaction during impact and particle melting. Spherical ice particles and water are used as analogs for the powder and melt pool, respectively, and are imaged using high-speed cameras during particle impact and subsequent melting into the liquid medium. To facilitate the comparison between a DED and the model system, we matched key dimensionless parameters as closely as possible, as summarized in Table 1. Insights from this study will enhance our understanding of the impact and phase change dynamics during DED and support the advancement of additive manufacturing processes.

Table 1: Comparison of typical DED parameters and corresponding test parameters in the model system (taken at 23-70°C), along with relevant non-dimensional numbers defined as Re: Reynolds number, We: Weber number, Bo: Bond number, Ja: Jakob number, Ca: Capillary number where g is gravity [m/s^2], C_p is specific heat capacity [kJ/kg.K] and h_{fs} is the enthalpy of fusion [kJ/kg].

Parameter	DED	Model system	Non-dimensional number	DED	Model system
Particle size (D) [μm]	25 – 120 (10,11)	2000	$Re = \frac{\rho v D}{\mu}$	200 – 2000	3900 – 4650
Impact speed (v) [m/s]	6 – 12 (11)	0.8 – 2.1	$We = \frac{\rho v^2 D}{\gamma}$	3.5 – 70	20 – 122
Liquid surface tension γ [mN/m]	1700 (12,13)	64 – 72 (14)	$Bo = \frac{\rho g D^2}{\gamma}$	<< 1	0.5 – 0.6
Liquid density ρ [kg/m^3]	7000 (13)	978 – 998 (15)	$Ja = \frac{C_p \Delta T_s}{h_{fs}}$	0.52 – 0.98	0.29 – 0.88

Liquid viscosity μ [mPa.s]	~5 (16)	0.4 – 0.9 (17)	$Ca = \frac{\mu v}{\gamma}$	0.02 – 0.04	0.01 – 0.03
Pool superheat ΔT_s [°C]	50 – 600 (18–21)	23 – 70			

Melting of spherical particles has been studied for both metals and ice under forced convection flow (22–25). In these studies, heat transfer increases with flow rate and is highest and the leading and trailing edges of the spherical particles (22–24). Circulating wake is shown behind the particles (22–24). Sphere and droplet impact into a quiescent surface is also documented, with notable features like bubble entrapment (26–28) and vortices (29). Similarly, during droplet impact and coalescence in miscible liquids vortex ring propagation and splashing are observed (29–35). Past research has been limited to melting of spherical particles under constant flow rates or (isothermal) particle impact without phase change. With this investigation we set out to observe the relation between particle impact, melting, and the influence of temperature and impact velocity.

3. Experimental Setup

To create approximately spherical ice particles, de-ionized (DI) water was first boiled for de-gassing and dyed with blue food coloring. Using a 33G needle, equal-sized droplets ($D \approx 2$ mm) were deposited on a petri dish coated with *Glaco*, a commercially available superhydrophobic coating. The droplets were then placed in a freezer to form spherical ice particles of consistent size and shape. These ice particles then impacted onto a DI water bath. Water was selected for its transparency and miscibility with the ice particles. The water was contained in a square borosilicate glass tank to avoid optical distortions. The bath was illuminated with a white backlight (Metaphase 3.5'' x 6'' backlight LED) for optimal video quality. A Photron Fastcam Mini AX200 high-speed camera with a Canon 1-5x 65mm macro lens (1x setting) at a resolution of 17.5 µm/pix was used to record ice impact and melting dynamics. The camera was positioned on a tripod parallel to the floor and focused on the center of the water bath as shown in Fig. 1. High frame rates (10,000 to 15,000 fps) were used to record the moment of impact. Lower frame rates (60-120 fps) were used to record the entire duration of the ice particle melt. At select experimental settings, an Edgertronic SC1 color high-speed camera with a Nikon 105mm lens at a resolution of 22.3 µm/pix recorded the impact and melting dynamics in top-view to complement high-speed side-view information obtained with the Photron camera.

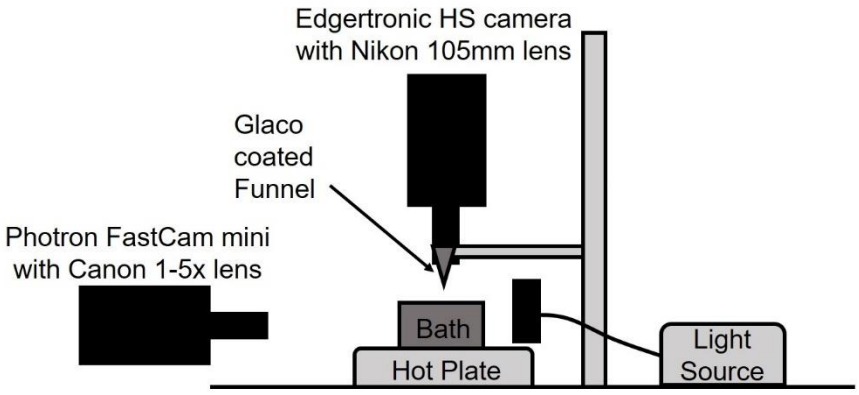

Figure 1: Schematic of the experimental setup

To ensure a consistent impact location and to minimize particle adhesion, the ice particles were directed using a Glaco-coated funnel. Ice spheres impacted from heights between 2 and 20 cm onto the water bath, resulting in impact velocities ranging from 0.8 to 2.1 m/s, as determined from additional high-speed videos just prior to impact. Velocities were averaged over several trials. For each impact height, the ice spheres impacted baths of six different temperatures T_{bath}: 23, 30, 40, 50, 60 and 70°C. To heat the bath, the glass tank was placed on a hotplate, and a type J/K thermocouple ensured a consistent bath temperature. Three trials were conducted for each temperature-velocity combination.

4. Methods

To analyze particle melt dynamics and melting times, videos were processed using ImageJ. To isolate the ice particle from the background, we determined an intensity threshold for each recording and converted the individual frames to binary images. We assumed that this threshold remained constant for the duration of each video, given the constant lighting intensity for the duration of the recording. The black pixel count was then converted to an equivalent area A_{eq} using the known lens calibration (17.5 µm/pix). The equivalent volume can be determined as $V_{eq} = 4/3\sqrt{A_{eq}/\pi}$ and the equivalent diameter becomes $D_{eq} = \sqrt{4A_{eq}/\pi}$, assuming a spherical particle shape. This assumption has been previously used for metal spherical particle melt (24). Fig. 2 shows a typical evolution of the particle equivalent diameter for a particle impacting a water bath at 23°C at an impact velocity of 2.1 m/s. The temporal evolution of the equivalent diameter can be used to determine the average heat transfer rate during melting. The time-dependent Nusselt number is (36):

$$Nu = \frac{\rho_w h_{fs} D_{eq}}{2k_w \Delta T_s} \times \left|\frac{dD}{dt}\right|, \quad (1)$$

where ρ_w is density of water, k_w is the thermal conductivity of the bath, and $\Delta T_s = T_{bath} - T_{sat}$. Thermo-physical properties of the bath were evaluated at the film temperature $T_{film} = (T_{sat} + T_{bath})/2$, where T_{sat} = 0°C is the melting temperature of ice, and it was assumed that the dye has no effect on these properties. As shown in Fig. 2b, the Nusselt number remains approximately constant during the melting process for times larger than a critical cut-off time, indicated by the vertical red line in Fig. 2b. Inconsistency in the Nusselt number towards the beginning of the melting process can be attributed to errors in ImageJ particle recognition due to bubble entrapment, and non-uniform melting dynamics. Hence, in the remainder of this work, we report the time-averaged Nusselt number above the cut-off time.

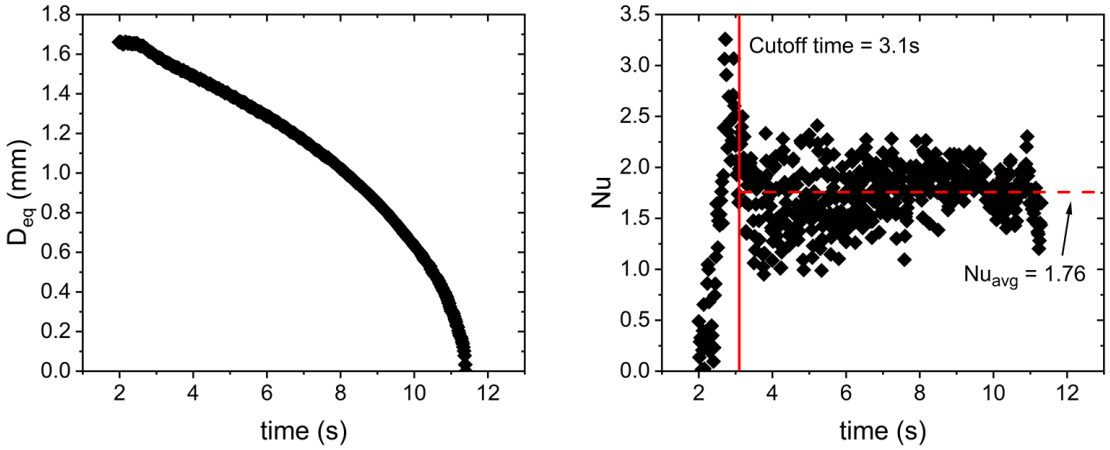

Figure 2: (a) Time evolution of the equivalent particle diameter upon melting for an ice particle impacting a water bath at room temperature (23°C) at a velocity of 2.1 m/s. (b) Nusselt number as derived from (a) using eq. (2), showing a stability cutoff at 3.1 seconds. Above the cut-off, Nusselt numbers are approximately constant with time over the course of the total melt period with an average Nusselt number of 1.76.

To estimate the error associated with assuming a spherical particle shape during image analysis, we divided the particle into horizontal and vertical 'pixel slices'. Each slice was rotated into a one-pixel thick cylinder, around the x or y axis. All cylinders were then added together to obtain a total volume. We found that throughout the melting, the error in volume between the spherical assumption and cylinder method was approximately 0.1 – 5%. This error is small enough that the spherical assumption is valid.

Error was also introduced when setting a threshold in ImageJ to distinguish the particle from background noise. Noise was most commonly seen along the particle edges and towards the bottom of the particle, where the melt water was similar in intensity to the ice. ImageJ was unable to distinguish between the melt plume and the un-molten particle, as shown in Fig. 3a, b. The automatically determined resulting pixel area was approximately 3% higher than the actual particle area, as shown with the red color in Fig. 3c. Overall, the uncertainty associated with setting a constant intensity threshold ranged from 3% to 8%. The relative error was generally higher at later stages of melting due to a reduced particle size.

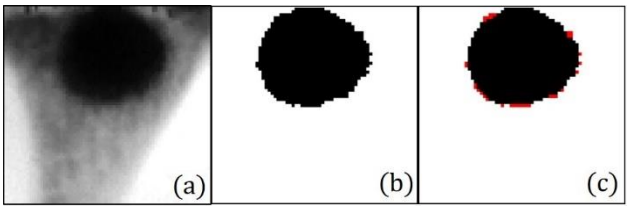

Figure 3: (a) ice particle (dark gray/black pixels) with melt water(light gray/white pixels) illuminated by Metaphase 3.5'' x 6'' backlight LED (b) processed image distinguishing the ice particle (black pixels) and melt/noise (white pixels) (c) processed image distinguishing the ice particle (black pixels), melt/noise (white pixels), and error associated with cutoff threshold (red pixels)

5. Results

5.1 Visual Observations

Ice particles and molten liquid dynamics displayed three different stages after impact. As seen in Fig. 4, the particle first penetrates and descends into the bath due to momentum from the initial impact (stage 1). The particle slows down due to drag and positive buoyancy of ice with respect to liquid water as it descends. After reaching a maximum penetration depth, the particle rises and resurfaces (stage 2). We observe particle rotation during impact and resurfacing. After resurfacing, the particle maintains its vertical position just below the bath surface until it melts completely (stage 3). The maximum impact depth of the ice particle becomes more variable with an increase in bath temperature. At lower bath temperatures (<50℃) the penetration depth is relatively constant for a given impact velocity. At high bath temperatures (>60℃), however, the penetration depth varies even for a given impact velocity. For example, at an impact velocity of 2.1 m/s, the particle impact depth ranges from 18.2mm to 24.6mm in a room temperature bath. However, in a 60℃ bath, the impact depth varies from 4.1 mm to 24.0 mm. In some instances, for higher bath temperatures (>60℃), the ice particle penetrates the bath but does not resurface; the particle is instead pulled downwards by convective currents. Other times, the particle barely penetrates the surface before resurfacing; it appears to be pushed upwards. This variability in impact dynamics indicates the presence of strong convective currents (*e.g.*, Rayleigh-Bénard convection) (37). At elevated temperatures, these currents overcome the inertial and buoyancy forces acting on the particle, and either pull the particle down or push it towards the surface.

During descent, a melt plume vortex forms in the wake behind the melting particle. The melt rises along the sides of the particle, forming circulating currents (vortex plumes) behind the particle as it travels downwards (Fig. 4). Vortex formation in the wake of a fluid flow around spheres is well documented (22,30). Hao and Tao observed that two circulating cells form in the wake of the flow around ice spheres, increasing heat transfer (22). Additionally, during droplet impact on a quiescent surface vortices form at the leading edge of the droplet upon impact (29). Here, the melt water appears to be originating from the upstream area (bottom) of the particle, and then recirculating towards the top of the particle. This observation indicates that the highest heat transfer rates (and hence melting rates) are indeed located near the leading edge of the particle due to forced convection. We also expect high heat transfer rates near the trailing edge due to the recirculating currents. This observation is consistent with findings of Hao and Tao (23), who show that local Nusselt numbers around a stationary spherical ice particle subject to laminar flow in a channel are highest at both the most upstream and downstream points of the particle.

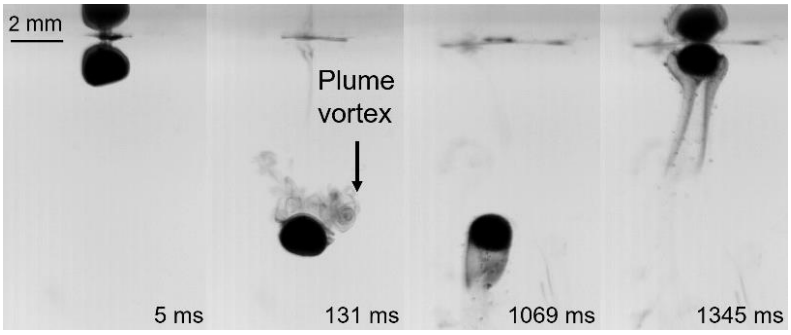

Figure 4: Side-view images of ice particle impact, plume vortex formation, and resurfacing for an impact velocity of 1.5 m/s and room temperature bath. Ice particles are dyed with food color to visualize the mixing dynamics of the melt with the surrounding water.

Figs. 5 shows the typical dynamics of the molten liquid for bath temperatures <50°C after the initial penetration and plume vortex formation. At low bath temperatures (<50°C) the particles are approximately stationary after resurfacing. The particle maintains its position after resurfacing until it has fully melted. Upon impact, a circular melt plume spreads radially outwards from the particle. We hypothesize that this initial plume originates from liquid water that accumulates on the ice particle during in-flight heating and melting. In Fig. 5a, the ice particle resurfaces due to positive buoyancy approximately 1.4 seconds after impact. During this process, the melt plume forms a vortex rings which continues to spread radially outwards from the particle, while traveling down in the reservoir due to the higher density of the cold ice melt. The melt continues to sink in single stream, expanding radially when hitting the bottom of the tank. Interestingly, throughout the entire melting process, the molten liquid follows the same path.

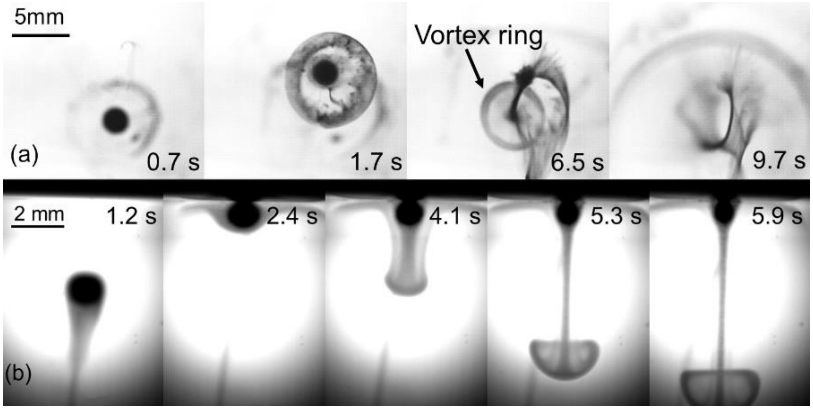

Figure 5: (a) Top-view images, showing the temporal evolution of the melt plume for an ice particle impacting a bath at room temperature with an impact velocity of 1.1 m/s (b) Side view images, showing the temporal evolution of the melt plume for a particle impacting a bath at room temperature with an impact velocity of 1.1 m/s illuminated by a fiber optic white light for higher illumination

A similar circular vortex ring was first documented by Thompson and Newall (33) in 1885 for droplet impact into liquid baths and has been studied since (31,32,34,38). Rodriguez and Mesler (34) note the formation of a vortex ring when droplets coalesces with the pool upon initial impact, instead of splashing. Interestingly, it is observed that vortex rings also form when the droplet coalesces without kinetic energy, *i.e.*, when gently placed on the surface, indicating that surface tension is a driving mechanism in ring formation (38). While the progression of this vortex ring has been described elsewhere, our observations of vortex rings from ice melt raise questions about the previously proposed explanations. Ray *et al.* (35) observed crater formation upon droplet impact; this crater eventually retracted to form the vortex ring. Rodrigues and Mesler (32) propose that upon impact, fluid on the leading edge of the droplet circulates outwards it as enters the pool, creating a rotating volute and internal circulating currents. A crater expands behind the droplet and retracts. The volute motion forms a symmetrical vortex ring which expands as it travels down in the pool (35). The ring decelerates during descent until reaching a maximum depth (31). The vortex rings that we observe (Fig. 5) are consistent with those previously described. However, our findings question the physical mechanism behind this

vortex ring formation. We observe vortex ring formation after impact and resurfacing. While vortex plumes form during the first impact stage (Fig. 4), they appear on the trailing edge of the particle. This is unlike the volutes that Rodrigues and Mesler (32,34) believe to drive ring formation. Additionally, the particles we use are solid, which eliminate the possibility of internal circulating currents. We propose instead that shear forces between the sinking colder (denser) melt and the warmer (less dense) fluids could be the reason for this vortex ring formation.

At higher temperatures (>50℃) we observe random ice particle motion during the melting process. After resurfacing (stage 3), the particle moves randomly across the surface of the bath. We hypothesize that the same convective currents (*i.e.*, Rayleigh-Bénard convection), which lead to the variability in maximum impact depth, are responsible for this ice particle motion. Furthermore, at elevated temperatures the melt plume is irregularly shaped (Fig. 6). Even upon initial impact, the radially outflowing plume is not symmetrical and varies in shape between different experimental runs. Nonetheless, even with the movement of the ice particle, the melt still follows the same path and sinks to the bottom of the tank, where it spreads into a distorted oval shape.

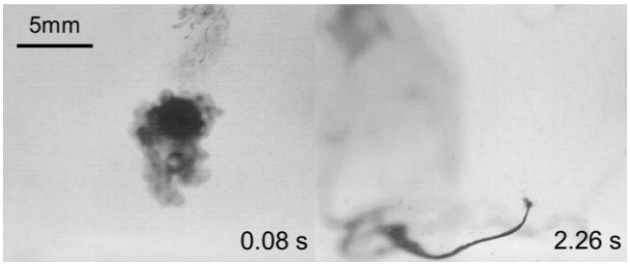

Figure 6: Top-view images, showing the temporal evolution of the melt plume for an ice particle impacting a bath at 70°C with velocity 1.1 m/s.

The melting dynamics in Fig. 5,6 indicate that the molten liquid does not fully mix with the bath by the time it has melted. The melt water follows a distinct path and does not deviate from its initial trajectory. At high temperatures (>50℃) the melt mixes to a greater degree than at lower bath temperatures. However, the melt plume still maintains a path and shape resembling a vortex ring that travels towards the bottom of the bath. In additive manufacturing, lack of mixing and thermal gradients can lead to inhomogeneous alloying and non-isotropic material and mechanical properties (1,39). Using Cu-based metallic glass powder on a Zr-based glass substrate, Sun and Flores note incomplete mixing of particles, as indicated by a color variation in the microstructure, resulting in a "mixed and unmixed melt zone" (40). Currently AM manufactured parts require secondary processing such as surface finishing or heat treatment, due to this part anisotropy (1).

In addition to the melt plume and vortex formation, we also observe bubble formation trailing the particle at higher impact velocities (v > 1.0 m/s) during impact and initial decent (stage 1), as shown in Fig. 7. During impact, a funnel shaped air cavity forms on the trailing (top) edge of the particle, similar to that documented by Akers and Belmonte for isothermal particle impact (26). As the distance between particle and liquid-gas interface increases, this cavity pinches off, leading to an entrapped bubble at the trailing edge of the particle. Aristoff *et al.* studied this cavity formation and found that at higher impact velocities, cavity formation and bubble entrapment were more consistent (28). Indeed, at lower

velocities (<1.0 m/s) we did not observe bubble formation, whereas at impact velocities greater than 1.0 m/s bubble entrapment was common, as seen in Fig. 7. In additive manufacturing, this entrapped bubble can cause porosity in a solidified workpiece. While controlled porosity may be desirable in certain applications, such as biomedical implants where interconnected voids enable cell proliferation (41), porosity is more often a concern due to its negative effect on mechanical properties, particularly fatigue resistance (42,43).

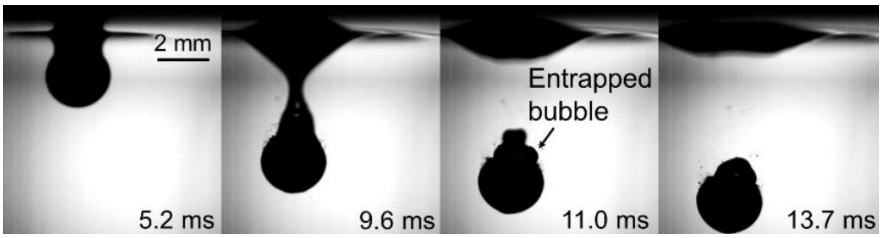

Figure 7: Side-view snapshot of particle impacting bath a room temperature bath at 1.8 m/s. Bubble entrapment and particle-surface interaction observed.

5.2 Heat transfer

After the qualitative analysis of the impact and melt dynamics, we quantified melting times and heat transfer rates. Melt times were determined for each particle impact. At each velocity-temperature combination 3 experiments were conducted. The averaged melt times are listed in table 2 (in seconds). As expected, as the bath temperature increases the particle melt time decreases. With a 47℃ increase in temperature, the particle melt time decreases by around 7 seconds, from 9.7 s at 23°C to 2.4 s at 70°C for impact at 0.8 m/s.

Table 2: Average melt times (seconds) with standard deviation for ice particles impacting heated baths for different temperature-velocity combinations.

Melt Time (s)		Temperatures (℃)					
		23	30	40	50	60	70
Impact Velocity (m/s)	0.8	9.7 ± 0.7	6.2 ± 0.7	4.4 ± 0.4	3.6 ± 0.1	2.7 ± 0.4	2.4 ± 0.4
	1.1	8.7 ± 0.4	6.1 ± 0.4	4.4 ± 0.4	3.5 ± 0.4	2.2 ± 0.2	2.4 ± 0.1
	1.5	8.8 ± 0.5	6.0 ± 0.3	4.3 ± 0.5	2.9 ± 0.1	2.5 ± 0.3	1.6 ± 0.2
	1.8	8.7 ± 0.2	5.7 ± 0.7	4.0 ± 0.1	3.2 ± 0.4	2.6 ± 0.1	2.3 ± 0.3
	2.1	8.6 ± 0.8	5.6 ± 0.3	3.9 ± 0.2	3.2 ± 0.4	2.4 ± 0.4	2.1 ± 0.5

In general, melt times decreased between the lowest and highest impact velocity. Interestingly, there is not a consistent decrease in melt time between each increase in velocity. We had expected that – with all other variables constant – the particle melt time would decrease with increasing velocity, since forced convection and consequently heat transfer during impact are also expected to increase (25,44). Melissari and Argyropoulos (25) show a positive linear Nu-Re correlation for melting ice spheres in a flow channel. In our experiments, the bath temperature was kept consistent within a range of ± 0.5°C.

Even though a 33G needle was used to deposit all sized droplets prior to freezing, we did observe slight differences in frozen particle shape and size. We believe these small variations had a greater influence on melt times than the variations in impact velocity. Error in volume calculations assuming a spherical particle shape ranged between 0.1 to 5.0%. This error is small enough that the spherical assumption is valid for the entire duration of the melt. However, over short time intervals, such as during the initial stage of impact, the error becomes significant for small changes in size. During impact, particle rotation was observed. Particle rotation and asymmetry added additional uncertainty in our efforts to determine any unambiguous trend in melting times. Analysis of early melt times was inconclusive, and we were not able to determine a Nu-Re correlation for the early stages of impact. A more controlled environment would be needed to determine a correlation between impact velocity and heat transfer. Furthermore, as described in the previous section, the most melting occurred after resurfacing, which inherently is independent of impact velocity.

To generalize our findings regarding the influence of bath temperature on melt times, we used dimensionless analysis. Following the analysis outlined in section 4, we find that for spherical ice particle melting in a water bath (*i.e.*, after re-surfacing), the Nusselt number varies linearly with the Jakob number, as shown in Fig. 8.

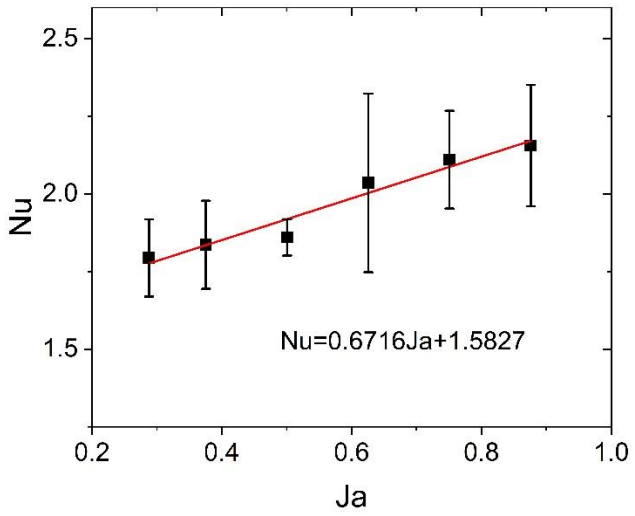

Figure 8: Dependence of Nusselt number on Jakob number for ice particle impact into water baths of different temperatures (averaged between 15 trials) with a linear regression and standard deviation error bars.

Using a linear regression, we find that:

$$Nu = 0.6716Ja + 1.5827, \tag{2}$$

This relationship is valid for spherical ice particles ($D \approx 2\ mm$) and bath temperatures between 23 and $70℃$. This correlation seems reasonable when compared to Nu numbers for free convection of solid spheres in water (45). Error in Nusselt number calculations fell between ± 0.11 and ± 0.28 for bath temperatures $\leq 40℃$, as indicated by the error bars in Fig. 8. At bath temperatures of $50℃$ and above the uncertainty reached as high as ± 0.57. We attribute the increase in uncertainty at higher

temperatures to the variations in particle dynamics, and thus heat transfer rates, in the presence of convective currents (see section 5.1). For high temperature applications like additive manufacturing, convective currents, such as Rayleigh-Bénard and Marangoni flow, could help explain particle melting and mixing inconsistencies.

6. Conclusion and outlook

Upon impact, particles penetrate the bath surface, reach a maximum penetration depth and resurface. During impact we observe bubble entrapment which occurs as the air cavity pinches off at the liquid-air interface. Plume vortices form in the circulating wake on the trailing edge of the particle during impact. After resurfacing we observe propagation of vortex rings. A circular plume initially spreads out along the bath surface. The plume sinks downwards into the bath as it expands in radius. Melt water in the vortex ring emerges from a single melt path that remains distinct for the duration of the melt. At higher bath temperatures, particle movement and melt plume distortion indicate the presence of convective currents. The melt path remains distinct even as a nonlinear shape at high temperatures. Melting times were shown to decrease with temperature. Impact velocity did not have measurable effect on melt times or heat transfer, due to variation in particle size and bath temperature. A positive linear correlation between Jakob and Nusselt numbers was derived, with increasing uncertainty at higher bath temperatures.

Our findings offer first insights into melting dynamics during particle impact into a heated bath or melt pool, which help explain some of the defects and inhomogeneities observed during direct energy deposition metallic additive manufacturing. Future research should focus on baths with higher lateral temperature gradients, so that in addition to the here-observed Rayleigh-Bénard convection the effect of Maragoni convection on melting and mixing can be studied (21,46). Furthermore, the effect of the high surface energy of molten liquid and the possible existence of a thin oxide layer warrant further investigations.

References

1. Thompson SM, Bian L, Shamsaei N, Yadollahi A. An overview of Direct Laser Deposition for additive manufacturing; Part I: Transport phenomena, modeling and diagnostics. Addit Manuf. 2015;8:36–62.

2. Gu DD, Meiners W, Wissenbach K, Poprawe R. Laser additive manufacturing of metallic components: materials, processes and mechanisms. Int Mater Rev. 2012 May;57(3):133–64.

3. Guo N, Leu MC. Additive manufacturing: technology, applications and research needs. Front Mech Eng. 2013 Sep;8(3):215–43.

4. Shah K, Pinkerton AJ, Salman A, Li L. Effects of Melt Pool Variables and Process Parameters in Laser Direct Metal Deposition of Aerospace Alloys. Mater Manuf Process. 2010 Dec 3;25(12):1372–80.

5. Semak VV, Hopkins JA, McCay MH, McCay TD. Melt pool dynamics during laser welding. J Phys Appl Phys. 1995 Dec 14;28(12):2443–50.

6. Scharowsky T, Osmanlic F, Singer RF, Körner C. Melt pool dynamics during selective electron beam melting. Appl Phys A. 2014 Mar;114(4):1303–7.

7. Sames WJ, List FA, Pannala S, Dehoff RR, Babu SS. The metallurgy and processing science of metal additive manufacturing. Int Mater Rev. 2016 Jul 3;61(5):315–60.

8. Volpp J, Dietz T, Vollertsen F. Particle Property Impact on its Distribution During Laser Deep Alloying Processes. Phys Procedia. 2014;56:1094–101.

9. Bartkowiak K. Direct laser deposition process within spectrographic analysis in situ. Phys Procedia. 2010;5:623–9.

10. Kovalev OB, Kovaleva IO, Smurov IYu. Numerical investigation of gas-disperse jet flows created by coaxial nozzles during the laser direct material deposition. J Mater Process Technol. 2017 Nov;249:118–27.

11. Smurov I, Doubenskaia M, Grigoriev S, Nazarov A. Optical Monitoring in Laser Cladding of Ti6Al4V. J Therm Spray Technol. 2012 Dec;21(6):1357–62.

12. Barker IJ. Surface Tension during Molten Metal Granulation. Metall Mater Trans B. 2007 Jul 20;38(3):351–6.

13. Li Z, Mukai K, Zeze M, Mills KC. Determination of the surface tension of liquid stainless steel. J Mater Sci. 2005 May;40(9–10):2191–5.

14. Vargaftik N, Volkov B, Voljak L. International tables of the surface tension of water. J Phys Chem Ref Data. 1983;12(3):817–20.

15. Haar L. NBS/NRC steam tables. CRC Press; 1984.

16. Korolczuk-Hejnak M, Migas P. Analysis of Selected Liquid Steel Viscosity / Analiza Lepkosci Wybranych Gatunków Stali W Stanie Ciekłym. Arch Metall Mater [Internet]. 2012 Jan 1 [cited 2017 Dec 8];57(4). Available from: http://www.degruyter.com/view/j/amm.2012.57.issue-4/v10172-012-0107-3/v10172-012-0107-3.xml

17. Kestin J, Sokolov M, Wakeham WA. Viscosity of liquid water in the range− 8 C to 150 C. J Phys Chem Ref Data. 1978;7(3):941–8.

18. Morville S, Carin M, Peyre P, Gharbi M, Carron D, Le Masson P, et al. 2D longitudinal modeling of heat transfer and fluid flow during multilayered direct laser metal deposition process. J Laser Appl. 2012 Aug;24(3):032008.

19. Manvatkar V, De A, DebRoy T. Spatial variation of melt pool geometry, peak temperature and solidification parameters during laser assisted additive manufacturing process. Mater Sci Technol. 2015 Jun;31(8):924–30.

20. Wang L, Felicelli S. Analysis of thermal phenomena in LENS^{TM} deposition. Mater Sci Eng A. 2006 Nov;435–436:625–31.

21. He X, Mazumder J. Transport phenomena during direct metal deposition. J Appl Phys. 2007 Mar;101(5):053113.

22. Hao Y, Tao Y. Melting of a Solid Sphere Under Forced and Mixed Convection: Flow Characteristics. Vol. 123. 2001.

23. Hao Y, Tao Y-X. Heat transfer characteristics of melting ice spheres under forced and mixed convection. J Heat Transf. 2002;124(5):891–903.

24. Kumar A, Roy S. Heat transfer characteristics during melting of a metal spherical particle in its own liquid. Int J Therm Sci. 2010;49(2):397–408.

25. Melissari B, Argyropoulos SA. Measurement of magnitude and direction of velocity in high-temperature liquid metals. Part I: Mathematical modeling. Metall Mater Trans B. 2005 Oct 1;36(5):691–700.

26. Akers B, Belmonte A. Impact dynamics of a solid sphere falling into a viscoelastic micellar fluid. J Non-Newton Fluid Mech. 2006 May 30;135(2):97–108.

27. MARSTON JO, VAKARELSKI IU, THORODDSEN ST. Bubble entrapment during sphere impact onto quiescent liquid surfaces. J Fluid Mech. 2011;680:660–70.

28. Aristoff JM, Truscott TT, Techet AH, Bush JWM. The water entry of decelerating spheres. Phys Fluids. 2010 Mar 1;22(3):032102.

29. Agbaglah G, Thoraval M-J, Thoroddsen ST, Zhang LV, Fezzaa K, Deegan RD. Drop impact into a deep pool: vortex shedding and jet formation. J Fluid Mech. 2015;764:R1.

30. Sakamoto H, Haniu H. A study on vortex shedding from spheres in a uniform flow. J Fluids Eng. 1990;112(4):386–92.

31. Shankar PN, Kumar M. Vortex rings generated by drops just coalescing with a pool. Phys Fluids. 1995 Apr 1;7(4):737–46.

32. Rodriguez F, Mesler R. The penetration of drop-formed vortex rings into pools of liquid. J Colloid Interface Sci. 1988 Jan 1;121(1):121–9.

33. Thomson JJ, Newall HF. V. On the formation of vortex rings by drops falling into liquids, and some allied phenomena. Proc R Soc Lond. 1886;39(239–241):417–36.

34. Rodriguez F, Mesler R. Some drops don’t splash. J Colloid Interface Sci. 1985 Aug 1;106(2):347–52.

35. Ray B, Biswas G, Sharma A. Vortex Ring Formation on Drop Coalescence With Underlying Liquid. 2013;(55492):V003T21A012.

36. Al Issa S, Weisensee P, Macian-Juan R. Experimental investigation of steam bubble condensation in vertical large diameter geometry under atmospheric pressure and different flow conditions. Vol. 70. 2014. 918–929 p.

37. Valencia L, Pallares J, Cuesta I, Grau FX. Rayleigh-Bénard convection of water in a perfectly conducting cubical cavity: Effects of temperature-dependent physical properties in laminar and turbulent regimes. Numer Heat Transf Part Appl. 2005 Feb 2;47(4):333–52.

38. Shariff K, Leonard A. Vortex rings. Annu Rev Fluid Mech. 1992;24(1):235–79.

39. Bian L, Thompson S, Shamsaei N. Mechanical Properties and Microstructural Features of Direct Laser-Deposited Ti-6Al-4V. Vol. 67. 2015.

40. Sun H, Flores KM. Laser deposition of a Cu-based metallic glass powder on a Zr-based glass substrate. J Mater Res. 2008;23(10):2692–703.

41. M. Mahamood R, Akinlabi E, Shukla DM, Pityana S. Characterizing the Effect of Processing Parameters on the Porosity of Laser Deposited Titanium Alloy Powder. In: Proceedings of the International MultiConference of Engineers and Computer Scientists 2014 Vol II, IMECS 2014,. Hong Kong; 2014.

42. Thompson SM, Bian L, Shamsaei N, Yadollahi A. An overview of Direct Laser Deposition for additive manufacturing; Part I: Transport phenomena, modeling and diagnostics. Addit Manuf. 2015 Oct;8:36–62.

43. Ng GKL, Jarfors AEW, Bi G, Zheng HY. Porosity formation and gas bubble retention in laser metal deposition. Appl Phys A. 2009 Nov;97(3):641–9.

44. Kramers H. Heat transfer from spheres to flowing media. physica. 1946;12(2–3):61–80.

45. Amato WS, Chi T. Free convection heat transfer from isothermal spheres in water. Int J Heat Mass Transf. 1972 Feb 1;15(2):327–39.

46. Wei PS, Liu HJ, Lin CL. Scaling weld or melt pool shape induced by thermocapillary convection. Int J Heat Mass Transf. 2012 Apr;55(9–10):2328–37.